ADVANCING EARTH AND SPACE SCIENCE

Geophysical Research Letters

RESEARCH LETTER
10.1029/2021GL097559

Key Points:

- We demonstrate the first electron microburst observation by spinning Electron Losses and Fields INvestigation CubeSats
- We present a comparison between ducted and nonducted chorus-driven electron precipitation
- Simulation shows ducted chorus cause electrons microbursts over energy 100s keV and above

Correspondence to:

L. Chen,
lunjin.chen@gmail.com

Citation:

Chen, L., Zhang, X.-J., Artemyev, A., Angelopoulos, V., Tsai, E., Wilkins, C., & Horne, R. B. (2022). Ducted chorus waves cause sub-relativistic and relativistic electron microbursts. *Geophysical Research Letters*, *49*, e2021GL097559. https://doi.org/10.1029/2021GL097559

Received 19 DEC 2021
Accepted 23 FEB 2022

Ducted Chorus Waves Cause Sub-Relativistic and Relativistic Electron Microbursts

Lunjin Chen[1], Xiao-Jia Zhang[2], Anton Artemyev[2,3], Vassilis Angelopoulos[2], Ethan Tsai[2], Colin Wilkins[2], and Richard B. Horne[4]

[1]Department of Physics, University of Texas at Dallas, Richardson, TX, USA, [2]Department of Earth, Planetary, and Space Sciences, University of California, Los Angeles, Los Angeles, CA, USA, [3]Space Research Institute, RAS, Moscow, Russia, [4]British Antarctic Survey, Cambridge, UK

Abstract During magnetospheric storms, radiation belt electrons are produced and then removed by collisions with the lower atmosphere on varying timescales. An efficient loss process is microbursts, strong, transient precipitation of electrons over a wide energy range, from tens of keV to sub-relativistic and relativistic energies (100s keV and above). However, the detailed generation mechanism of microbursts, especially over sub-relativistic and relativistic energies, remains unknown. Here, we show that these energetic electron microbursts may be caused by ducted whistler-mode lower-band chorus waves. Using observations of equatorial chorus waves nearby low-altitude precipitation as well as data-driven simulations, we demonstrate that the observed microbursts are the result of resonant interaction of electrons with ducted chorus waves rather than nonducted ones. Revealing the physical mechanism behind the microbursts advances our understanding of radiation belt dynamics and its impact on the lower atmosphere and space weather.

Plain Language Summary The Van Allen radiation belts, donut-shaped rings of relativistic electrons, encircle Earth at distance ~3–7 Earth radii. During magentospheric storms, radiation belt electrons are produced and then removed by collisions with the lower atmosphere on varying timescales. Resonant electron interaction with whistler-mode chorus waves has long been known as one of the most important mechanisms of electron precipitation into the atmosphere. An efficient loss process is microbursts, strong, transient precipitation of electrons over a wide energy range. To scatter and precipitate energetic electrons, however, chorus waves should propagate to middle latitudes. Here, we show that such a wave propagation and the subsequent microburst generation can be possible under wave ducting, that is, wave energy being trapped within localized plasma density enhancements. Revealing the physical mechanism behind the microbursts advances our understanding of radiation belt dynamics and its impact on the lower atmosphere and space weather.

1. Introduction

Concurrently operating acceleration, transport, and loss of relativistic electrons cause the Earth's radiation belt dynamics (Turner et al., 2014). Electromagnetic whistler-mode chorus waves, characterized by frequency chirping below the electron gyrofrequency (Ω_{ce}), are widely thought to be critical to both acceleration and scattering of energetic electrons in the Earth's radiation belts (Y. Chen et al., 2007). Although electron quasi-linear interaction with low-amplitude whistler waves can explain electron slow (hours-long timescale), diffusive transport (Thorne et al., 2013), electron nonlinear interaction with intense chorus waves (Breneman et al., 2017) is thought to drive rapid, strong electron precipitation, known as microbursts (Douma et al., 2017; O'Brien et al., 2004). In either regime, the efficiency of electron scattering by whistler waves depends on wave intensity and wavefield distribution along magnetic field lines (O. V. Agapitov et al., 2018; Thorne et al., 2005; Wang & Shprits, 2019).

As electrons trapped by the Earth's dipole field bounce along magnetic field lines, their parallel velocity ($v_\parallel$) varies with magnetic latitude (λ) while the magnetic moment is conserved. As the electron plasma frequency-to-gyrofrequency ratio decreases with λ, the wavenumber (k) decreases (and the phase velocity increases) in accordance with the whistler wave dispersion relation. This results in an increase of the minimum resonant energy of interaction at higher latitudes (Horne & Thorne, 2003), because the resonance condition with field-aligned chorus waves requires $v_\parallel = (\omega - \Omega_{ce}/\gamma)/k_\parallel$ (ω and γ are the wave frequency and the relativistic factor, respectively). Microburst precipitations occur in a broad energy range, from tens of keV to hundreds of keV (Mozer et al., 2018; Shumko et al., 2018), and even up to MeV (Blum et al., 2015). They are so strong that they can dominate relativistic electron losses (Thorne et al., 2005) deep inside the radiation belts (far from the magnetosphere boundary). Inclusion of such precipitation in radiation belt models is challenging, however. Although the most intense field-aligned chorus waves have been shown to be confined around the geomagnetic equator ($|\lambda| < 20°$) (Meredith et al., 2012; O. V. Agapitov et al., 2013), losses of relativistic electrons in microbursts require resonant scattering at middle to high latitudes, $|\lambda| > 30°$, based on the aforementioned minimum resonant energy dependence on latitude. The minimum resonant energy is higher for high-order cyclotron resonances of electrons with oblique chorus waves (propagating at a large angle with respect to the background magnetic field), and such high-order resonances may contribute to the near-equatorial scattering of electrons that form microbursts (see Lorentzen et al., 2001). However, oblique waves are much less intense than field-aligned waves (e.g., O. V. Agapitov et al., 2018) due to Landau damping by suprathermal electrons (see Bortnik et al., 2007; L. Chen et al., 2013). Electron scattering by resonance with electromagnetic ion cyclotron waves may produce microbursts, but only at ultrarelativistic energies (Kubota et al., 2015). So most microbursts, which occur over a wide energy range (a few keV to MeV), cannot be explained.

Unlike typical chorus waves, which are localized around the equator, a distinct population of chorus waves can propagate to high latitudes (Colpitts et al., 2020) and even to the ground (Demekhov et al., 2017; Martinez-Calderon et al., 2016) without the increasing obliquity that would result in damping and divergence from magnetic field lines. These are referred to as ducted chorus waves, as they are trapped within local plasma density enhancements or depletions and propagate mostly along magnetic field lines (Helliwell, 1965). Although whistler-mode wave ducting has been largely attributed to strong plasma density gradients near the plasmapause (Inan & Bell, 1977), recent numerical simulations have shown that even low-amplitude density perturbations can duct waves in the radiation belt (Hanzelka & Santolík, 2019; Hosseini et al., 2021). The ducted chorus have been shown to be capable of producing bursts of electron precipitation over a wide range of energy (e.g., L. Chen et al., 2020). Are these ducted chorus waves required to account for observed sub-relativistic and relativistic microbursts (100s keV and above)? To address this question, we use spacecraft observations of chorus waves around the equator and electron precipitation at low altitudes, and numerical simulations of electron precipitation driven by realistically propagating chorus waves.

2. Observation

Electron Losses and Fields INvestigation (Angelopoulos et al., 2020), ELFIN in short, comprises twin spinning CubeSats (ELFIN-A and ELFIN-B) with an ~3s spin period that can measure both precipitating and trapped electron fluxes within a half spin. The two ELFIN CubeSats operate in a low-altitude (~400 km) circular orbit with an orbital period of ~90 min. The electron Energetic Particle Detector onboard ELFIN provides complete electron pitch-angle distributions at 50–7,000 keV (16 differential channels) with an energy resolution of $\Delta E/E < 50\%$, an angular resolution of ~22.5° (i.e., 16 sectors per spin), and a time resolution of 1.5 s (i.e., half spin); the raw sector data are at a higher time resolution of ~190 ms to examine precipitation on shorter timescales.

Figure 1 shows an overview of the event with low-altitude electron precipitation measured by ELFIN-A CubeSat and intense chorus wave measurement from near-equatorial Van Allen Probe A observations (Mauk et al., 2013). ELFIN-A observed precipitating and trapped fluxes of energetic (>50 keV) electrons at a low altitude, ~450 km. One can see a series of enhanced precipitation flux bursts around 14:01:10 UT (Figure 1a) while trapped electron fluxes do not show such individual enhancements (Figure 1b). The ratio of these two fluxes shows strong precipitation seen as two bursts in the outer radiation belt. These precipitation bursts occur over a wide energy range from 50 to ~700 keV. After 14:01 UT the flux ratio is near 1 and above, which is well localized in time, that is, ELFIN captured intense bursts of precipitating electrons. The high precipitating-to-trapped ratio over a wide range of energies, but with a short timescale, are signatures of microbursts and nonlinear wave-particle interaction. The bursts of high precipitating-to-trapped ratio (see Figure 1c) show that the precipitating flux increase is caused not by increased equatorial fluxes, but by rapid electron losses.

Van Allen Probe A (Mauk et al., 2013) crossed the equatorial region in the same *L*-shell range on the dayside, as ELFIN-A. Figure 1g shows a projection of Van Allen Probes and ELFIN orbits to the *L*-shell and MLT plane (projections of ELFIN orbits in dipole and Tsyganenko-Sitnov (Tsyganenko & Sitnov, 2005) magnetic field models show uncertainties of mapping). Wave measurements from the waveform receiver (WFR) on the Electric

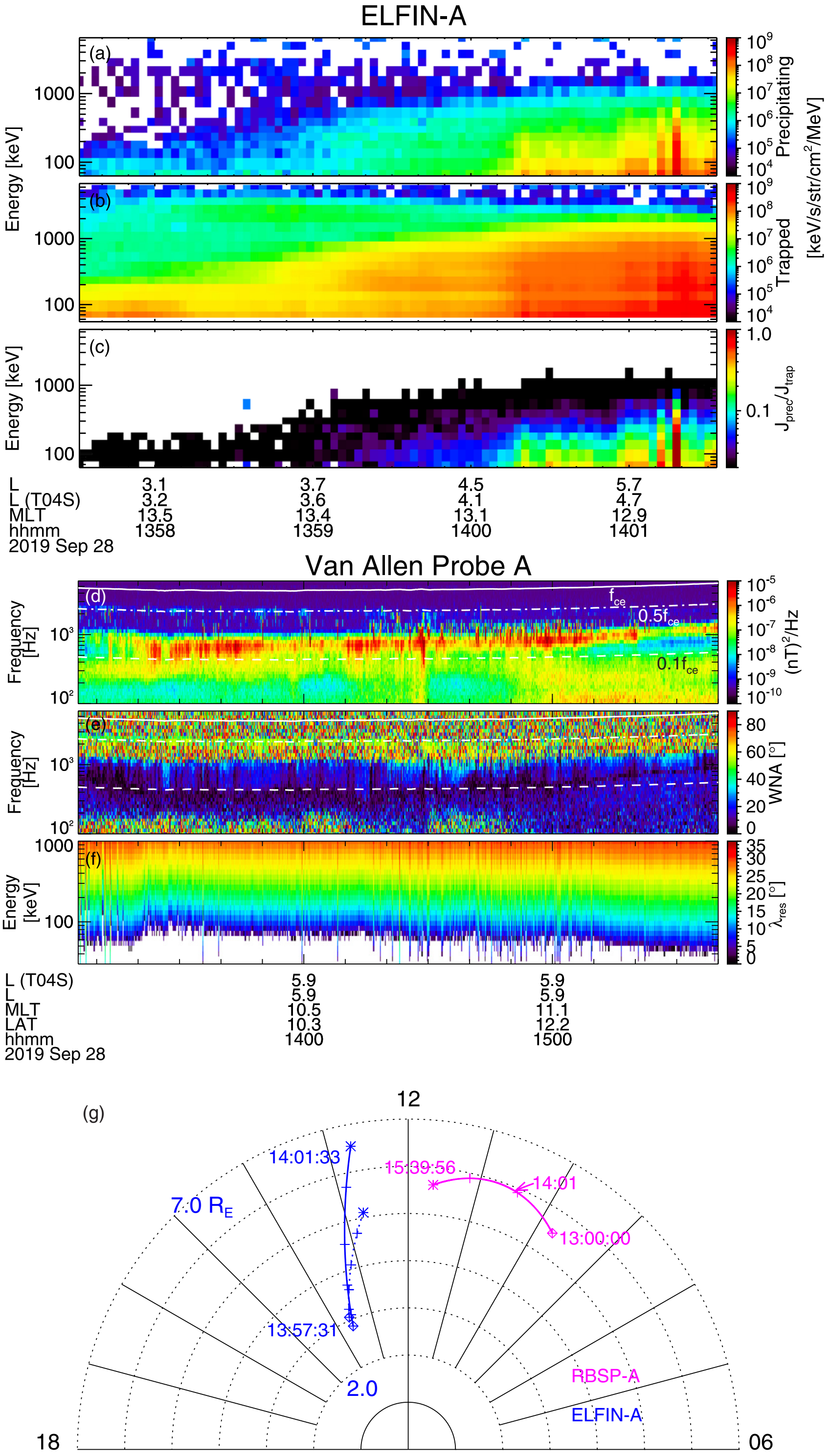

Figure 1. Energy spectra of (a) precipitating and (b) trapped electrons and (c) the ratio of these two spectra as measured by Electron Losses and Fields INvestigation-A (ELFIN-A) on 28 September 2019. (d) Wave magnetic field spectrum and (e) wave normal angle spectrum measured by Van Allen Probe A. The white solid, dashed-dotted, and dashed lines in panels (d and e) indicate local electron gyrofrequency f_{ce} and $f_{ce}/2$, and $f_{ce}/10$, respectively. (f) Resonance latitude of different energies for the wave frequency corresponding to the peak whistler-mode wave intensity. (g) Van Allen Probe A orbit in (L-shell, MLT) plane as well as ELFIN-A orbit projected along dipole (blue solid line) and Tsyganenko-Sitnov (Tsyganenko & Sitnov, 2005) (blue dotted line) models separately. Positions of ELFIN-A and Van Allen Probe A (L-shell, magnetic local time and magnetic latitude) are shown in panels (c and f), respectively.

and Magnetic Field Instrument and Integrated Science (EMFISIS) wave instrument (Kletzing et al., 2013) onboard the Van Allen Probes A shows whistler-mode chorus waves near the magnetic equator. These waves were seen during the entire interval of Van Allen Probe A observations (in the vicinity of ELFIN-A's *L*-shell). Despite that the MLT difference between Van Allen Probe A and ELFIN-A (~2 hr) is slightly larger than the averaged spatial scale of the day-side chorus source region, 1–1.5 hr in MLT (O. Agapitov et al., 2018), Van Allen Probe A observed chorus wave activities for nearly 2 hr while it moved even closer to ELFIN-A's MLT and thus it is reasonable to assume the waves responsible for the precipitation at ELFIN share similar properties to those captured by Van Allen Probe A. The WFR instrument provides magnetic and electric field spectra and polarization properties (Santolík et al., 2003) over 65 frequency channels from 10 Hz to 12 kHz with a 6s cadence (Kletzing et al., 2013). ELFIN quickly crossed the *L*-shell range of intense whistler-mode chorus waves (Figure 1d) as observed by Van Allen Probe A with field-aligned propagation (with wave normal angle <20° as shown in Figure 1e).

To estimate electron resonance latitude with these waves, we solved the resonance condition ($v_{\parallel} = (\omega - \Omega_{ce}/\gamma)/k_{\parallel}$) and the whistler-mode wave dispersion relation. For the dispersion relation, we assumed a dipole magnetic field topology, whose local values match DC magnetic field measurements from the magnetometer in the EMFISIS instrumentation suite, and a constant density profile along a field line with total plasma density from the upper hybrid resonance frequency (Kurth et al., 2015) captured by the high-frequency receiver. Figure 1f shows the calculated resonant latitude as a function of kinetic energy of electrons near the loss cone. If these waves reach sufficiently high latitudes ($\lambda \sim 30°$), they may resonate with 50–700 keV electrons and generate microbursts (see Figure 1f). Wave propagation to such latitudes with high intensity would require wave ducting by local plasma density gradients. It is challenging, however, for equatorial spacecraft to directly capture small density ducts (evidence of ducted propagation) due to uncertainties in cold plasma density measurements. During the event from Figure 1, Van Allen Probe A shows some density gradients in the data derived from the upper hybrid resonance frequency (Kurth et al., 2015), but the uncertainties are too large to clearly demonstrate which gradients might be related to whistler waves. Therefore, we perform two simulations (one with ducted waves and the other with nonducted waves) in Section 3 to confirm that only electron scattering by ducted waves could have reproduced the microbursts observed by ELFIN-A.

To better show the timescale of these precipitation bursts from Figure 1, we examine the original subspin (~188 ms) measurements from ELFIN. Figure 2 shows electron fluxes from ~two spins, encompassing the strongest precipitation burst at ~14:01:18 UT. During the spinning, different pitch angles are measured at each time (Figure 2a). For pitch angles within the loss cone (those pitch angles that are larger than the local loss cone of ~110°, as indicated by the shaded region near the center of Figure 2), the measured flux corresponds to precipitation. The precipitating flux increased by more than an order of magnitude over that in the adjacent half spin (Figure 2b). The timescale of this precipitation burst is close to the time resolution of these data (3/16 ~ 0.2 s), as is typical of individual microbursts (Blum et al., 2015; O'Brien et al., 2004). The measured precipitating-to-trapped flux ratio at half-spin resolution in Figure 2c shows enhanced precipitation lasting 1–2 s, which may consist of multiple microbursts like the one mentioned above. For the period of enhanced precipitation, the measured flux ratio can exceed unity below 200 keV and decreases with increasing electron energy.

Waveform data from WFR during its regular burst mode, which lasts for 0.5 s during each capture (at a cadence of 35,000 samples/s), is available to reveal a fine-scale chorus element during the interval from Figure 1. Figures 3a and 3b show the wave spectra and an example of high-resolution (35 kHz sampling frequency) wave packet measurements by Van Allen Probe A. The peak wave amplitude is very large (reaching ~400 pT), and the wave propagates almost along magnetic field lines (wave intensity is dominated by transverse components). This chorus element will be used drive the test particle simulation below, to test the hypothesis that the observed microbursts are caused by ducted chorus waves.

3. Simulation

To examine the role of ducted chorus waves in microburst generation, we numerically evaluate precipitation caused by wave-particle interactions with ducted and nonducted waves. For both wave models, we adopt the ray-tracing technique to reconstruct wavefield distributions in time and space (Bortnik et al., 2003) from a spatially localized wave source at the equator, constrained by observed wave characteristics. In the first model,

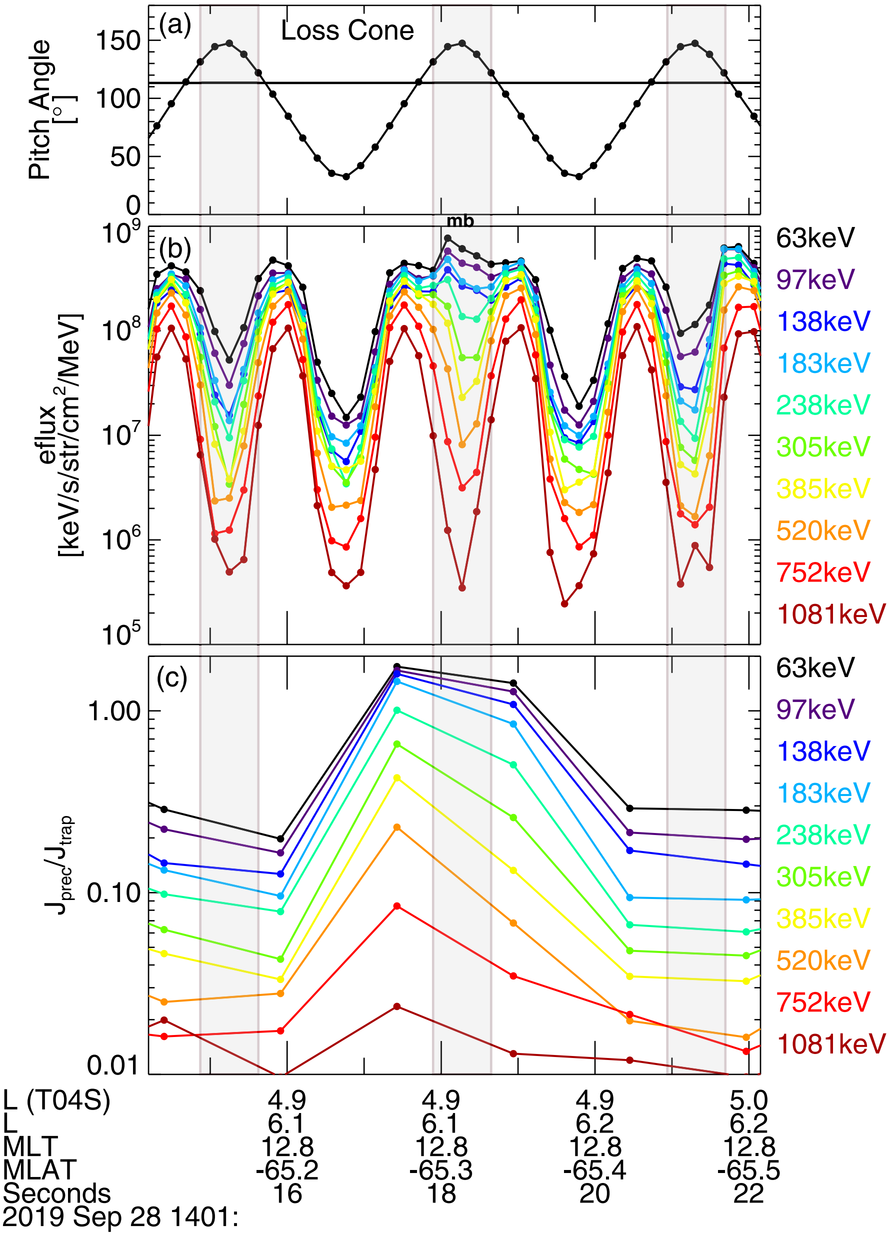

Figure 2. High-resolution measurements from two spins of Electron Losses and Fields INvestigation around the precipitation burst at ~14:01:18 UT: (a) instantaneous pitch angle of each measurement, (b) energy flux at different energies (color-coded). (c) Precipitating-to-trapped flux ratio (J_{prec}/J_{trap}) at half-spin resolution (same as in Figure 1c). In panel (a), the pitch angle corresponding to the local loss cone (~110°) in the southern hemisphere is marked by the horizontal line. When the instantaneous pitch angle appears above the loss cone, measurement of precipitating electrons (i.e., those within the loss cone) are made and are highlighted as shaded areas in gray.

ducted wave propagation with the wave-normal angle set strictly to zero is assumed; in the second model, the wave normal angle evolves according to ray-tracing equations in an inhomogeneous plasma medium embedded with a dipolar magnetic field. The modeled electromagnetic fields of chorus waves are then used to trace the motion of an ensemble of test particles (L. Chen et al., 2020), from which electron fluxes are calculated.

To model electron response to modeled (ducted and nonducted) chorus wave fields at a given *L*, test particle equations (Equations 1–4 of L. Chen et al. (2020)) are solved. For the presented event, ~4.8 × 10^7 electrons are launched at $L = 6$, with 51 electron energies in logarithmic spacing from 50 keV to 1 MeV, 65 equatorial pitch angles ranging from the edge of the loss cone (~3°) to 10°, 120 gyrophases, and 120 different bounce

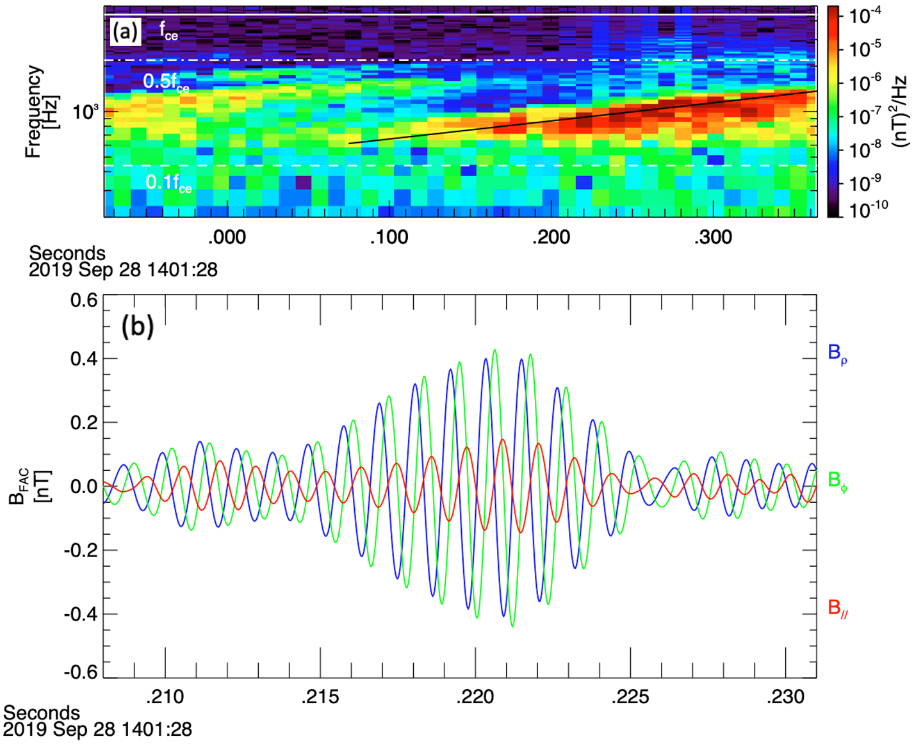

Figure 3. (a) Chorus wave spectra from the high-resolution (burst-mode) waveform measurements at Van Allen Probe A (Mauk et al., 2013). (b) Example chorus waves with wave magnetic fields in local field-aligned coordinates.

phases (occupying electron bounce paths). Each test particle represents an ensemble of electrons whose number is assigned according to the average flux observed by Van Allen Probe A around the closest conjunction (13:59:45 to 14:01:15 UT). These electrons' momentum and locations are traced and used to reconstruct electron unidirectional differential flux as a function of energy, pitch angle, and time, with details described in L. Chen et al. (2020). A virtual satellite is placed at ELFIN-A's altitude in the southern hemisphere to capture the variation in electron fluxes.

Chorus wave fields are modeled by ray tracing in a prescribed magnetized plasma medium. For the medium, we use a dipolar magnetic field and a diffusive equilibrium density model (Bortnik et al., 2011) with a scaling factor introduced so the plasma density matches the observed plasma density from Van Allen Probe A, 3 cm^{-3}. The following ray-tracing equations (e.g., Horne, 1989; L. Chen et al., 2021) are solved

$$\frac{d\mathbf{R}}{dt} = -\frac{\partial D}{\partial \mathbf{k}} \Big/ \frac{\partial D}{\partial \omega} \tag{1}$$

$$\frac{d\mathbf{k}}{dt} = \frac{\partial D}{\partial \mathbf{R}} \Big/ \frac{\partial D}{\partial \omega} \tag{2}$$

$$\frac{d\omega}{dt} = 0 \tag{3}$$

$$\frac{dA}{dt} = -\gamma_L A \tag{4}$$

where $D(\mathbf{k}, \omega, \mathbf{R}) = 0$ is the local whistler-mode dispersion relation, and $\mathbf{k}$ and A are the wave vector and wave magnetic amplitude, respectively, along the ray path $\mathbf{R}$. In Equation 4, γ_L represents the Landau damping rate due to electrons over suprathermal energy range ($\sim$0.1 $-$ 26 keV), whose distribution is statistically parameterized by L-shell, MLT, and Planetary K-index (Kp) (L. Chen et al., 2012). The wave phase along the ray path is obtained as $\phi(t) = \int \mathbf{k} \cdot d\mathbf{R} - \omega t$. For the special case of ducted chorus waves, $\mathbf{k}_\perp = 0$ is assumed so that Landau damping vanishes ($\gamma_L = 0$), and Equation 2 is reduced to an equation for $k_\parallel$, $D(k_\parallel, \omega, \mathbf{R}) = 0$, where the subscripts $_\perp$ and $_\parallel$ represent the components perpendicular and parallel to the background magnetic field, respectively.

To model electromagnetic fields of ducted chorus waves for the presented event, rays are traced from the equator to $\lambda = 40°$ at $L = 6$ with initial wave vectors along the field line and with 81 different wave frequencies from 600 to 1,400 Hz with a spacing of 10 Hz. The launch time depends on wave frequency, according to an observed discrete frequency chirping from 610 to 1,360 Hz over 0.3 s (denoted by the black line in Figure 3a). The initial wave amplitude profile A_0 is set such that A_0 is a constant of 300 pT over 890–1,100 Hz and falls off at higher and lower frequencies with a spectral Gaussian width of 150 and 130 Hz, respectively. The input discrete spectrum of the chorus waves is based on the observed discrete spectrum shown in Figure 3a. The wave phase and wave amplitude along these 81 rays are used to interpolate electromagnetic fields as a function of time and position so test particle equations can be solved (L. Chen et al., 2020).

Rays launched over different L-shells are required to model electromagnetic fields of nonducted chorus waves, because they can propagate across L-shells. In addition to 81 different frequencies, rays are also launched at the equator at 51 different L values from 5.75 to 6.25 with a spacing of 0.01. In total, 4,131 rays are traced. In addition to the frequency dependence mentioned above, the initial wave amplitude A_0 contains a Gaussian L-dependence, with the peak at $L = 6$ and a width of $\Delta L = 0.05$. This width corresponds to 320 km, a typically observed width (Shen et al., 2019). The wave phase, wave amplitude, and wave normal angles along these 4,131 rays are used to interpolate and obtain nonducted chorus electromagnetic fields as a function of time and position, which then are used for tracing test particles.

Figure 4 shows a comparison of ray-tracing results for ducted and nonducted chorus waves. Unlike ducted chorus waves, nonducted chorus waves tend to be refracted toward a larger L-shell ($L \sim 6.2$). Furthermore, nonducted chorus waves become highly oblique with wave normal angle $\theta > 60°$ when reaching $\lambda = 20°$; as a result of Landau damping caused by suprathermal electrons, these waves are attenuated by 20 dB there. Therefore, the nonducted chorus wave intensity is well confined below $\lambda = 20°$ near $L \sim 6.2$.

Figures 5a and 5b shows precipitating and trapped electron fluxes at ELFIN-A's altitude from the simulation with ducted chorus waves. The chorus wave spectrum at the equator is set up according to the observed frequency chirping and with zero wave normal angle. There are no precipitating fluxes prior to the scattering by chorus waves (the loss cone is empty), but trapped fluxes are always present. Resonant interaction with chorus waves perturbs both trapped and precipitating fluxes, and the latter result in a partial or fully filled loss cone, depending on electron energy. Figure 5c shows the ratio of precipitating-to-trapped fluxes, which can be as high as 2 at 60 keV and decreases with increasing energy. The ratio exceeding unity demonstrates nondiffusive transport in pitch angle, a signature of nonlinear wave-particle interaction (L. Chen et al., 2020). As chorus waves propagate away from the equator, they resonate with progressively larger energies when reaching higher latitudes. The precipitating-to-trapped flux ratio reaches one and above for a wide energy range up to ~300 keV, and decrease to 0.4 at ~700 keV. Such a high flux ratio within the energy range up to 700 keV agrees well with ELFIN observations of the most intense microburst precipitation in Figure 1. Note that the observed flux ratios may contain uncertainties, because precipitating and trapped fluxes were measured at different sectors (i.e., non-simultaneously) as ELFIN spins (see Figure 2). These scattering signatures from ducted chorus waves agree well with ELFIN observations of microburst precipitation. Also noteworthy is that both observed trapped (just outside the loss cone) and precipitating fluxes are enhanced around the precipitation bursts (Figure 2b), which demonstrates electron transport in the pitch-angle direction and is also reproduced by the modeling (Figures 5a and 5b).

In Figures 5d–5f, we show the modeled electron precipitation by nonducted chorus waves for comparison with the results for ducted chorus waves in Figures 5a–5c. Test particle simulation in the nonducted chorus wave fields is performed at $L = 6.2$. Waves are initialized at the equator with the same spectrum as the ducted chorus waves. As the waves propagate to higher latitudes, the wave normal angle becomes more oblique and Landau damping due to suprathermal electrons takes effect. The damping quickly reduces the wave intensity by two orders of magnitude at $\lambda \sim 20°$ (Figure 4). These waves can effectively scatter and precipitate <100 keV electrons around the equator. Unlike the intensity of the chorus waves, however, that of the nonducted chorus waves at middle latitudes is insufficient to drive strong precipitation of >100 keV electrons. There are very few flux perturbations for >300 keV electrons, and resonance with them requires chorus waves at even higher latitudes.

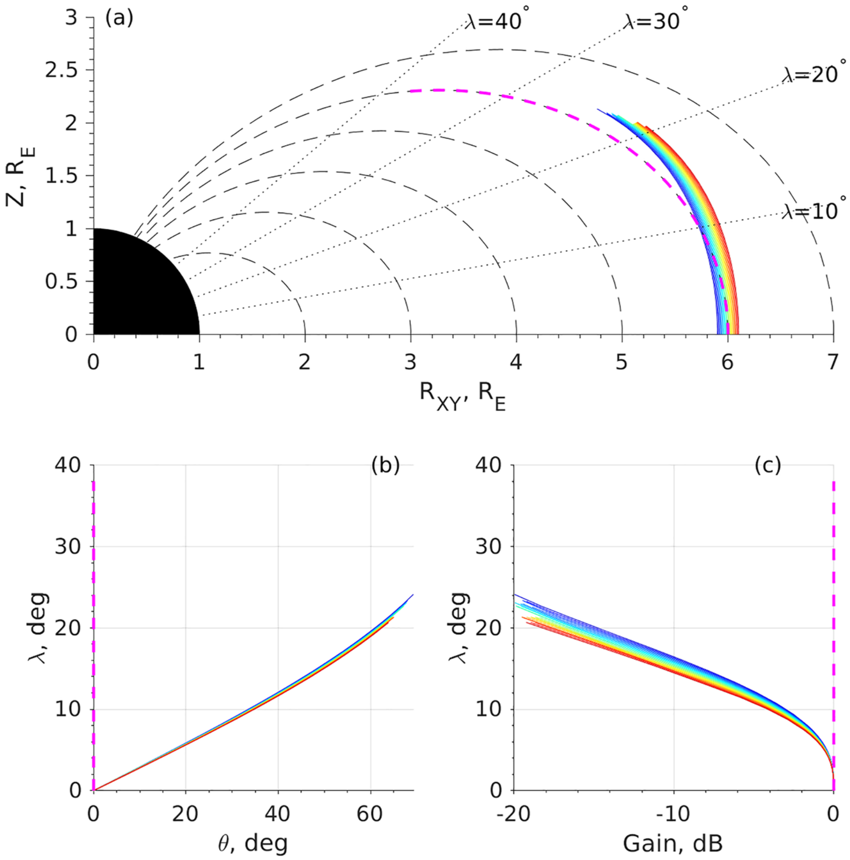

Figure 4. Comparison of ducted wave model with nonducted wave model for a fixed wave frequency at 1 kHz. (a) Modeled ray paths and (b) modeled wave normal angle θ versus magnetic latitude λ. (c) Modeled wave gain in dB versus λ. A ducted ray is represented by magenta lines, and nonducted rays are represented by jet colors with colors denoting initial L values of the launch locations.

A comparison of ELFIN observations (Figure 2) to model simulations (Figure 5) of microburst precipitation shows a similar energy ranges of precipitating electrons in the case with ducted chorus waves. Without wave ducting, even very intense chorus waves (the wave amplitude was ~300 pT at the equator in the presented event) cannot produce sufficiently strong electron scattering above 100 keV to explain those observed microbursts. Thus, microburst precipitation may require not only intense chorus waves to be generated around the equator, but also plasma density fluctuations responsible for wave ducting to middle and high latitudes, because higher-energy (>100–700 keV) microbursts are caused by electron scattering at such latitudes.

4. Summary and Discussion

We present a unique observation of electron microbursts from ELFIN and long-lasting, large-scale chorus wave source regions from Van Allen Probes. Constraint by the chorus wave observation from Van Allen Probes, electron precipitation driven by ducted and nonducted chorus waves is compared. Comparison with EFLIN electron microburst observation demonstrates ducted lower-band chorus waves are responsible for the observed microbursts.

The significant role of ducted chorus waves in sub-relativistic and relativistic electron scattering and precipitation indicates that these waves deserve particular attention and should be treated as a separate wave population. Although they occur less often than predominantly nonducted whistler-mode waves (Gu et al., 2021), ducted waves are much more efficient to drive microbursts. The resultant microbursts can quickly empty radiation belts (Douma et al., 2019; Greeley et al., 2019; Thorne et al., 2005) and change the radiation environment during geomagnetically active conditions. Therefore, accurate parametrization and inclusion of ducted chorus waves

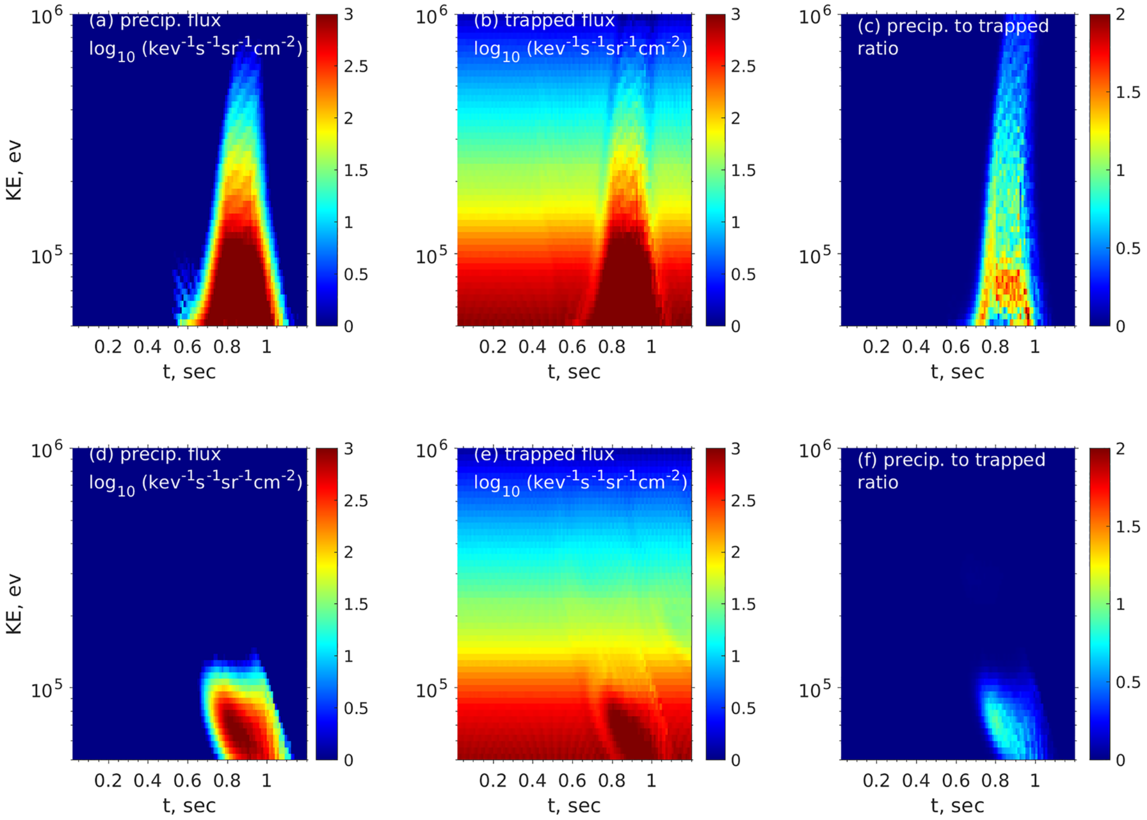

Figure 5. Modeled (a) precipitating fluxes, (b) trapped fluxes, and (c) precipitating-to-trapped flux ratio at Electron Losses and Fields INvestigation-A's altitude from the model with ducted chorus waves. The time t is relative to the time when chorus waves are launched. Most microburst precipitation (up to 1 MeV) is seen at around $t \sim 0.8$ s and lasts for ~0.2 s. Panels (d–f) are similar to panels (a–c) except for the simulation with nonducted chorus waves. The main microburst precipitation (below ~100 keV) is seen at around $t \sim 0.8$ s and lasts for ~0.2 s.

in radiation belt models is required to provide realistic results of energetic electron loss. Our demonstration of ducted chorus waves as the driver of electron microbursts provides valuable experimental data for controllable remediation of hazard radiation environment by injecting man-made radio waves (Scherbarth et al., 2009). The discovered microburst mechanism shows a pathway of radiation belt electron precipitation, which affects atmospheric chemistry and connect to ground-level climate (Baker et al., 2018) and has a great implication on understanding the variabilities of radiation belts of other planets.

Acknowledgments

L. Chen acknowledges support by the NASA grants 80NSSC21K1688 and 80NSSC21K1320. X.-J. Zhang, A. Artemyev, and V. Angelopoulos acknowledge support by the NASA award 80NSSC20K1578 and the NSF grants NSF-2021749, AGS-1242918, AGS-2019950, and AGS-2021749. The authors are grateful to teh NASA's CubeSat Launch Initiative for ELFIN's successful launch in the desired orbits. The authors acknowledge early support of ELFIN project by the AFOSR, under its University Nanosat Program, UNP-8 project, contract FA9453-12-D-0285, and the California Space Grant program. The authors acknowledge critical contributions of numerous volunteer ELFIN team student members.

Data Availability Statement

ELFIN data is available at http://themis-data.igpp.ucla.edu/ela/. The authors acknowledge the Van Allen Probes EMFISIS data obtained from https://emfisis.physics.uiowa.edu/data/index, MagEIS data obtained from http://www.rbsp-ect.lanl.gov/data_pub/. Data access and processing was done using SPEDAS V4.1, see Angelopoulos et al. (2019).

References

Agapitov, O., Mourenas, D., Artemyev, A., Mozer, F. S., Bonnell, J. W., Angelopoulos, V., et al. (2018). Spatial extent and temporal correlation of chorus and hiss: Statistical results from multipoint THEMIS observations. *Journal of Geophysical Research: Space Physics*, *123*(10), 8317–8330. https://doi.org/10.1029/2018JA025725

Agapitov, O. V., Artemyev, A., Krasnoselskikh, V., Khotyaintsev, Y. V., Mourenas, D., Breuillard, H., et al. (2013). Statistics of whistler mode waves in the outer radiation belt: Cluster STAFF-SA measurements. *Journal of Geophysical Research*, *118*(6), 3407–3420. https://doi.org/10.1002/jgra.50312

Agapitov, O. V., Mourenas, D., Artemyev, A. V., Mozer, F. S., Hospodarsky, G., Bonnell, J., & Krasnoselskikh, V. (2018). Synthetic empirical chorus wave model from combined Van Allen Probes and cluster statistics. *Journal of Geophysical Research: Space Physics*, *123*(1), 297–314. https://doi.org/10.1002/2017JA024843

Angelopoulos, V., Cruce, P., Drozdov, A., Grimes, E. W., Hatzigeorgiu, N., King, D. A., et al. (2019). The space physics environment data analysis system (SPEDAS). *Space Science Reviews*, *215*(1), 9. https://doi.org/10.1007/s11214-018-0576-4

Angelopoulos, V., Tsai, E., Bingley, L., Shaffer, C., Turner, D. L., Runov, A., et al. (2020). The ELFIN mission. *Space Science Reviews*, *216*(5), 103. https://doi.org/10.1007/s11214-020-00721-7

Baker, J. B., Erickson, P. J., Fennell, J. F., Foster, J. C., Jaynes, A. N., & Verronen, P. T. (2018). Space weather effects in the Earth's radiation belts. *Space Science Reviews*, *214*(1), 17. https://doi.org/10.1007/s11214-017-0452-7

Blum, L. W., Li, X., & Denton, M. (2015). Rapid MeV electron precipitation as observed by SAMPEX/HILT during high-speed stream-driven storms. *Journal of Geophysical Research*, *120*(5), 3783–3794. https://doi.org/10.1002/2014JA020633

Bortnik, J., Chen, L., Li, W., Thorne, R. M., & Horne, R. B. (2011). Modeling the evolution of chorus waves into plasmaspheric hiss. *Journal of Geophysical Research*, *116*(A8), 8221. https://doi.org/10.1029/2011JA016499

Bortnik, J., Inan, U. S., & Bell, T. F. (2003). Frequency-time spectra of magnetospherically reflecting whistlers in the plasmasphere. *Journal of Geophysical Research*, *108*(A1), 1030. https://doi.org/10.1029/2002JA009387

Bortnik, J., Thorne, R. M., Meredith, N. P., & Santolik, O. (2007). Ray tracing of penetrating chorus and its implications for the radiation belts. *Geophysical Research Letters*, *34*(15), L15109. https://doi.org/10.1029/2007GL030040

Breneman, A. W., Crew, A., Sample, J., Klumpar, D., Johnson, A., Agapitov, O., et al. (2017). Observations directly linking relativistic electron microbursts to whistler mode chorus: Van Allen Probes and FIREBIRD II. *Geophysical Research Letters*, *44*(22), 11265–11272. https://doi.org/10.1002/2017GL075001

Chen, L., Bortnik, J., Li, W., Thorne, R. M., & Horne, R. B. (2012). Modeling the properties of plasmaspheric hiss: 1. Dependence on chorus wave emission. *Journal of Geophysical Research*, *117*(A5). https://doi.org/10.1029/2011JA017201

Chen, L., Breneman, A. W., Xia, Z., & Zhang, X.-J. (2020). Modeling of bouncing electron microbursts induced by ducted chorus waves. *Geophysical Research Letters*, *47*(17), e89400. https://doi.org/10.1029/2020GL089400

Chen, L., Thorne, R. M., Li, W., & Bortnik, J. (2013). Modeling the wave normal distribution of chorus waves. *Journal of Geophysical Research*, *118*(3), 1074–1088. https://doi.org/10.1029/2012JA018343

Chen, L., Zhang, X.-J., Artemyev, A., Zheng, L., Xia, Z., Breneman, A. W., & Horne, R. B. (2021). Electron microbursts induced by nonducted chorus waves. *Frontiers in Astronomy and Space Sciences*, *8*, 163. https://doi.org/10.3389/fspas.2021.745927

Chen, Y., Reeves, G. D., & Friedel, R. H. W. (2007). The energization of relativistic electrons in the outer Van Allen radiation belt. *Nature Physics*, *3*(9), 614–617. https://doi.org/10.1038/nphys655

Colpitts, C., Miyoshi, Y., Kasahara, Y., Delzanno, G. L., Wygant, J. R., Cattell, C. A., et al. (2020). First direct observations of propagation of discrete chorus elements from the equatorial source to higher latitudes, using the Van Allen Probes and Arase satellites. *Journal of Geophysical Research: Space Physics*, *125*(10), e28315. https://doi.org/10.1029/2020JA028315

Demekhov, A. G., Manninen, J., Santolík, O., & Titova, E. E. (2017). Conjugate ground-spacecraft observations of VLF chorus elements. *Geophysical Research Letters*, *4411*(23), 735744–735811. https://doi.org/10.1002/2017GL076139

Douma, E., Rodger, C. J., Blum, L. W., & Clilverd, M. A. (2017). Occurrence characteristics of relativistic electron microbursts from SAMPEX observations. *Journal of Geophysical Research: Space Physics*, *122*(8), 8096–8107. https://doi.org/10.1002/2017JA024067

Douma, E., Rodger, C. J., Blum, L. W., O'Brien, T. P., Clilverd, M. A., & Blake, J. B. (2019). Characteristics of relativistic microburst intensity from SAMPEX observations. *Journal of Geophysical Research: Space Physics*, *124*(7), 5627–5640. https://doi.org/10.1029/2019JA026757

Greeley, A. D., Kanekal, S. G., Baker, D. N., Klecker, B., & Schiller, Q. (2019). Quantifying the Contribution of microbursts to global electron loss in the radiation belts. *Journal of Geophysical Research: Space Physics*, *124*(2), 1111–1124. https://doi.org/10.1029/2018JA026368

Gu, W., Chen, L., Xia, Z., & Horne, R. B. (2021). Direct evidence reveals transmitter signal propagation in the magnetosphere. *Geophysical Research Letters*, *48*(15), e2021GL093987. https://doi.org/10.1029/2021GL093987

Hanzelka, M., & Santolík, O. (2019). Effects of ducting on whistler mode chorus or exohiss in the outer radiation belt. *Geophysical Research Letters*, *46*(11), 5735–5745. https://doi.org/10.1029/2019GL083115

Helliwell, R. A. (1965). *Whistlers and related ionospheric phenomena*. Stanford University Press.

Horne, R. B. (1989). Path-integrated growth of electrostatic waves – The generation of terrestrial myriametric radiation. *Journal of Geophysical Research*, *94*(A7), 8895–8909. https://doi.org/10.1029/JA094iA07p08895

Horne, R. B., & Thorne, R. M. (2003). Relativistic electron acceleration and precipitation during resonant interactions with whistler-mode chorus. *Geophysical Research Letters*, *30*(10), 100000–100001. https://doi.org/10.1029/2003GL016973

Hosseini, P., Agapitov, O., Harid, V., & Gołkowski, M. (2021). Evidence of small scale plasma irregularity effects on whistler mode chorus propagation. *Geophysical Research Letters*, *48*(5), e92850. https://doi.org/10.1029/2021GL092850

Inan, U. S., & Bell, T. F. (1977). The plasmapause as a VLF wave guide. *Journal of Geophysical Research*, *82*(19), 2819–2827. https://doi.org/10.1029/JA082i019p02819

Kletzing, C. A., Kurth, W. S., Acuna, M., MacDowall, R. J., Torbert, R. B., Averkamp, T., et al. (2013). The electric and magnetic field instrument suite and integrated science (EMFISIS) on RBSP. *Space Science Reviews*, *179*(1–4), 127–181. https://doi.org/10.1007/s11214-013-9993-6

Kubota, Y., Omura, Y., & Summers, D. (2015). Relativistic electron precipitation induced by EMIC-triggered emissions in a dipole magnetosphere. *Journal of Geophysical Research: Space Physics*, *120*(6), 4384–4399. https://doi.org/10.1002/2015JA021017

Kurth, W. S., De Pascuale, S., Faden, J. B., Kletzing, C. A., Hospodarsky, G. B., Thaller, S., & Wygant, J. R. (2015). Electron densities inferred from plasma wave spectra obtained by the waves instrument on Van Allen Probes. *Journal of Geophysical Research*, *120*(2), 904–914. https://doi.org/10.1002/2014JA020857

Lorentzen, K. R., Blake, J. B., Inan, U. S., & Bortnik, J. (2001). Observations of relativistic electron microbursts in association with VLF chorus. *Journal of Geophysical Research*, *106*(A4), 6017–6028. https://doi.org/10.1029/2000JA003018

Martinez-Calderon, C., Shiokawa, K., Miyoshi, Y., Keika, K., Ozaki, M., Schofield, I., et al. (2016). ELF/VLF wave propagation at subauroral latitudes: Conjugate observation between the ground and Van Allen Probes A. *Journal of Geophysical Research: Space Physics*, *121*(6), 5384–5393. https://doi.org/10.1002/2015JA022264

Mauk, B. H., Fox, N. J., Kanekal, S. G., Kessel, R. L., Sibeck, D. G., & Ukhorskiy, A. (2013). Science objectives and rationale for the radiation belt storm probes mission. *Space Science Reviews*, *179*(1–4), 3–27. https://doi.org/10.1007/s11214-012-9908-y

Meredith, N. P., Horne, R. B., Sicard-Piet, A., Boscher, D., Yearby, K. H., Li, W., & Thorne, R. M. (2012). Global model of lower band and upper band chorus from multiple satellite observations. *Journal of Geophysical Research*, *117*(A10), 10225. https://doi.org/10.1029/2012JA017978

Mozer, F. S., Agapitov, O. V., Blake, J. B., & Vasko, I. Y. (2018). Simultaneous observations of lower band chorus emissions at the equator and microburst precipitating electrons in the ionosphere. *Geophysical Research Letters*, *45*(2), 511–516. https://doi.org/10.1002/2017GL076120

O'Brien, T. P., Looper, M. D., & Blake, J. B. (2004). Quantification of relativistic electron microburst losses during the GEM storms. *Geophysical Research Letters*, *31*(4), L04802. https://doi.org/10.1029/2003GL018621

Santolík, O., Parrot, M., & Lefeuvre, F. (2003). Singular value decomposition methods for wave propagation analysis. *Radio Science*, *38*(1), 1010. https://doi.org/10.1029/2000RS002523

Scherbarth, M., Smith, D., Adler, A., Stuart, J., & Ginet, G. (2009). AFRL's demonstration and science Experiments (DSX) mission. In S. Fineschi & J. A. Fennelly (Eds.), *Solar Physics and Space Weather Instrumentation III* (Vol. 7438, pp. 101–110). SPIE. https://doi.org/10.1117/12.824898

Shen, X.-C., Li, W., Ma, Q., Agapitov, O., & Nishimura, Y. (2019). Statistical analysis of transverse size of lower band chorus waves using simultaneous multisatellite observations. *Geophysical Research Letters*, *46*(11), 5725–5734. https://doi.org/10.1029/2019GL083118

Shumko, M., Sample, J., Johnson, A., Blake, B., Crew, A., Spence, H., et al. (2018). Microburst scale size derived from multiple bounces of a microburst simultaneously observed with the FIREBIRD-II CubeSats. *Geophysical Research Letters*, *45*(17), 8811–8818. https://doi.org/10.1029/2018GL078925

Thorne, R. M., Li, W., Ni, B., Ma, Q., Bortnik, J., Chen, L., et al. (2013). Rapid local acceleration of relativistic radiation-belt electrons by magnetospheric chorus. *Nature*, *504*(7480), 411–414. https://doi.org/10.1038/nature12889

Thorne, R. M., O'Brien, T. P., Shprits, Y. Y., Summers, D., & Horne, R. B. (2005). Timescale for MeV electron microburst loss during geomagnetic storms. *Journal of Geophysical Research*, *110*(A9), 9202. https://doi.org/10.1029/2004JA010882

Tsyganenko, N. A., & Sitnov, M. I. (2005). Modeling the dynamics of the inner magnetosphere during strong geomagnetic storms. *Journal of Geophysical Research*, *110*(A3), A03208. https://doi.org/10.1029/2004JA010798

Turner, D. L., Angelopoulos, V., Li, W., Bortnik, J., Ni, B., Ma, Q., et al. (2014). Competing source and loss mechanisms due to wave-particle interactions in Earth's outer radiation belt during the 30 September to 3 October 2012 geomagnetic storm. *Journal of Geophysical Research*, *119*, 1960–1979. https://doi.org/10.1002/2014JA019770

Wang, D., & Shprits, Y. Y. (2019). On how high-latitude chorus waves tip the balance between acceleration and loss of relativistic electrons. *Geophysical Research Letters*, *46*(14), 7945–7954. https://doi.org/10.1029/2019GL082681